International Journal of Heat and Mass Transfer 52 (2009) 422–430

Contents lists available at ScienceDirect

International Journal of Heat and Mass Transfer

journal homepage: www.elsevier.com/locate/ijhmt

Conjugate numerical analysis of flow and heat transfer with phase change in a miniature flat plate CPL evaporator

Z.M. Wan [a,b,*], W. Liu [b], Z.K. Tu [b], A. Nakayama [c]

[a] Department of Physics, Hunan Institute of Science and Technology, Yueyang 414006, PR China
[b] School of Energy and Power Engineering, Huazhong University of Science and Technology, Wuhan 430074, PR China
[c] Department of Mechanical Engineering, Shizuoka University, 3-5-1 Johoku, Hamamatsu 432-8561, Japan

ARTICLE INFO

Article history:
Received 8 May 2007
Received in revised form 20 June 2008
Available online 18 August 2008

Keywords:
Capillary pumped loop
Flat plate evaporator
Porous wick
Side wall effect heat transfer limit

ABSTRACT

Two-dimensional numerical model for the global evaporator of miniature flat plate capillary pumped loop (CPL) is developed to describe heat and mass transfer with phase change in the porous wick, liquid flow and heat transfer in the compensation cavity and heat transfer in the vapor grooves and metallic wall. The governing equations for different zones are solved as a conjugate problem. The side wall effect heat transfer limit is introduced to estimate the heat transport capability of evaporator. The influences of liquid subcooling, wick material, metallic wall material and non-uniform heat flux on the evaporator performance are discussed in detail.

1. Introduction

With the advent of high performance and small satellite and spacecraft due to miniaturization technologies, the heat dissipation tendency of these systems is continually on the rise and there is a great challenge to dissipate ever-increasing heat fluxes. Because of high heat transfer capacity, two phase heat transfer technology is considered a promising solution for thermal management applications of such satellite and spacecraft. The capillary pumped loop (CPL) is one of the results of the two phase devices which transport heat using phase change [1,2]. As a derivative of the heat pipe, CPL is capable of transport large heat density and passively transporting heat over large distances with minimal temperature losses, and uses capillary action for fluid transport and contains no moving parts. Moreover heat is transferred along with evaporation and condensation, CPL is much more economical in terms of weight than conventional thermal control systems [3,4]. Therefore, CPL is especially well suited for thermal control applications of satellite and spacecraft with high heat fluxes [5,6]. At the same time, CPL also offers a great potential for terrestrial application, especially for electronics cooling [7].

Various aspects of theory and experiment of CPLs have been investigated in detailed for space application and electronics cooling [8]. However, most of these studies are concentrated on the CPLs with large size cylindrical evaporators. In order to utilize CPLs for thermal control of small satellite and spacecraft and for electronics cooling, their potential in the direction of miniaturization need to be evaluated. Because flat plate evaporator has the advantages of good thermal contact condition, low thermal resistance and isothermal heated surface [9], our primary interest in this work is miniature flat plate CPL.

Fig. 1 shows the schematic of miniature flat plate CPL. As seen, CPL is composed of an evaporator, a condenser, a reservoir, vapor, and liquid transport lines. During normal operation, heat is applied to the evaporator, leading to evaporation of the working fluid. A meniscus forms at the vapor–liquid interface inside the evaporator capillary structure and naturally adjusts itself to establish a capillary force that matches the total pressure loss in the CPL system [10]. The resulting vapor flows through the vapor grooves, out of the evaporator, through the vapor transport lines, and into the condenser, where it condenses into liquid. Liquid condensate continues to flow through the liquid transport lines and returns to the evaporator, completing the cycle. The capillary evaporator is the most important part in a CPL system because it is the heat absorbing element and provides the capillary force of fluid through the loop. The two-phase reservoir is used to control the temperature of the loop and accommodates fluid inventory shifts during changes in operating conditions. The wick in the condenser is used to provide a stable physical interface between the liquid and vapor phases, reduce or even eliminate the possible occurrence of pressure oscillations during operation [11].

Though the miniature CPL has the potential as a heat transfer device with high efficiency for thermal management of small spacecraft, the reduction of CPL evaporator size from current

* Corresponding author. Address: Department of Physics, Hunan Institute of Science and Technology, Yueyang 414006, PR China.
E-mail address: zhongminwan@hotmail.com (Z.M. Wan).

0017-9310/$ - see front matter © 2008 Elsevier Ltd. All rights reserved.
doi:10.1016/j.ijheatmasstransfer.2008.06.019

Nomenclature

c	Specific heat [J Kg^{-1} K^{-1}]
h_{fg}	Latent heat of evaporation [J kg^{-1}]
k	Thermal conductivity [W m^{-1} K^{-1}]
K	Permeability [m^2]
L_x	Total length in x-direction [m]
L_{x1}	Length between origin and left surface of wick [m]
L_{x2}	Length between origin and left surface of compensation cavity [m]
L_{x3}	Length of the bottom metallic wall [m]
L_y	Total height in y-direction [m]
L_{y1}	Height of the bottom metallic wall [m]
L_{y2}	Height of the bottom surface of wick [m]
L_{y3}	Height of the upper surface of wick [m]
P	Pressure [Pa]
ΔP_c	Capillary force [Pa]
q	Heat flux [W m^{-2}]
r_e	Effective capillary radius of wick porous [m]
t	Time [s]
T	Temperature [°C]
ΔT	Temperature difference [°C]
u	Velocity in x-direction [m s^{-1}]
v	Velocity in y-direction [m s^{-1}]
$\vec{V}$	Velocity vector [m s^{-1}]
n	Normal unit vector at the vapor–liquid interface

Greek symbols

ρ	Density [Kg m^{-3}]
ε	Porosity [%]
θ	Effective contact angle
μ	Viscosity [Pa s]
σ	Liquid–vapor surface tension [N m^{-1}]

Subscripts

a	Ambient
al	Aluminum
eff	Effective
in	Inlet
l	Liquid
mw	Metallic wall
ni	Nickel
s	Solid
st	Stainless steel
sat	Saturation
sub	Subcooling
sup	Superheating
v	Vapor

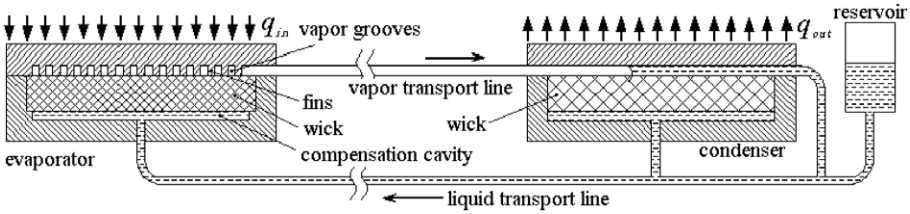

Fig. 1. Schematic of a miniature flat plate CPL system.

bigger to smaller dimensions has been slow, mainly due to insufficient understanding of the physical behaviors occurring within the evaporator. Consequently, the performance optimization and design of CPL requires a thorough understanding of physical behaviors occurring inside the evaporator.

Cao and Faghri [12] developed an analytical solution for heat and mass transfer processes during evaporation in the wick of a CPL evaporator. In this study, it was assumed that the entire porous structure was saturated with liquid and the liquid–vapor interface was located on the unheated portion of the upper surface. With these two assumptions, only the liquid flow in the porous media needed to be studied and the capillary pressure at the liquid–vapor interface was neglected. At the same year, Demidov and Yatsenko [13] presented a numerical study showing that vapor zones can take place within the wick in the capillary evaporator under the fins. Figus et al. [14] have also presented a numerical solution for heat and mass transfer in the cylindrical evaporator wick by using the Darcy model and by using a two-dimensional pore network model. An important conclusion of this work is that the pore network model results are nearly identical to those of the Darcy model for an ordered single pore-size distribution. Yan and Ochterbeck [15] provided a numerical study on the flow and heat transfer in the wick structure of evaporator for a CPL based on two-phase mixture model.

In the works mentioned above, the computational domain adopted is a single segment of wick structure in the evaporator. However, for a flat plate CPL, as shown in Fig. 2, the capillary evaporator consists of wick structure, metallic wall, vapor grooves, and compensation cavity. The computational domain mentioned above is only a very small part of wick, and it leads to some shortages in evaluating the overall evaporator performance by these models. Firstly, these models cannot predict the influences of metallic wall, vapor grooves, and compensation cavity on heat and mass transfer of the capillary evaporator, the heated surface temperature which is very important in estimating the performance of thermal management system cannot obtained, either. On the other hand, the effect of heat conduction of metallic wall is not considered, obviously, it is not appropriate in studying the evaporator characteristics, especially for a miniature flat plate CPL evaporator. Compared with the length of heated wall, the thickness of metallic side wall cannot be neglected. Due to the high thermal conductivity of metallic wall, the liquid inside the bottom of wick and the compensation cavity may possibly be heated up to a temperature that is greater than the saturation temperature corresponding to local saturation pressure by effect of heat conduction of metallic side wall, the vapor may potentially generate there as well, and vapor presence in there has been found to fully or partially block liquid flow to the vapor–liquid interface [16], which may lead eventually to dry-out of an evaporator and failure of CPL system. Therefore, the overall model is indispensable for understanding of the behavior of the capillary evaporator as a whole.

In this work, a global evaporator model of miniature flat plate CPL which couples liquid and vapor flow, heat transfer and phase change in the porous wick structure, heat transfer and flow in

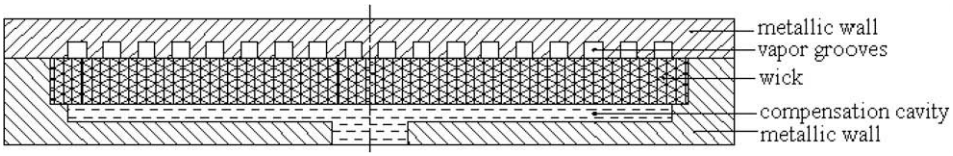

Fig. 2. Schematic of miniature flat plate evaporator.

the compensation cavity and heat transfer in the vapor grooves and metallic wall is presented. The entire evaporator was solved numerically with SIMPLE algorithm as a conjugate problem. The influences of heat load, liquid subcooling, wick material, metallic wall material and non-uniform heat fluxes on the evaporator performance are discussed in detail, and the side wall effect heat transfer limit caused by heat conduction of metallic side wall is investigated as well. To the best of our knowledge, the overall evaporator model has not been proposed before in the context of capillary evaporators.

2. Mathematical model

As the evaporator is taken to be symmetric, a half of evaporator cross section is selected as the computational domain, as shown in Fig. 3. The origin of the coordinate system is located at the left bottom corner of evaporator.

To develop the mathematical model, the main assumptions are made as follows:

(1) For simplicity, the vapor flow in the vapor grooves is neglected, and heat transfer is mainly by conduction.
(2) The porous media is rigid, homogenous, isotropic, and fully saturated with fluid. There is local thermodynamic equilibrium between solid phase and liquid or vapor phase.
(3) The fluid is incompressible and has the constant properties.

For the space environment, the effect of gravity is neglected. The heat and mass transfer for the liquid and vapor regions in the wick structure are based on the volume-averaged technique and Brinkman–Darcy–Forchheimer model of porous media.

The governing equations of the global evaporator can be written as follows.

(1) Metallic wall

$$(\rho c)_{\mathrm{mw}}\frac{\partial T}{\partial t} = k_{\mathrm{mw}}\left(\frac{\partial^2 T}{\partial x^2}+\frac{\partial^2 T}{\partial y^2}\right) \tag{1}$$

(2) Vapor grooves

$$(\rho c)_{\mathrm{v}}\frac{\partial T}{\partial t} = k_{\mathrm{v}}\left(\frac{\partial^2 T}{\partial x^2}+\frac{\partial^2 T}{\partial y^2}\right) \tag{2}$$

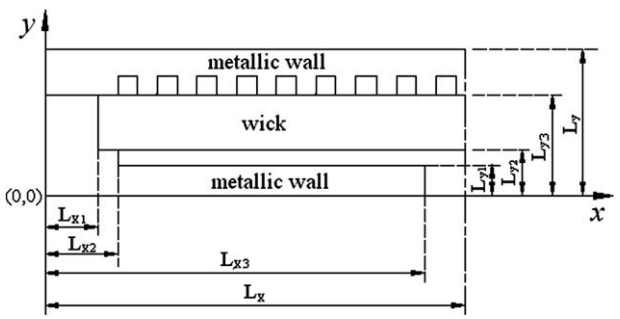

Fig. 3. Computation domain and coordinate system.

(3) Wick structure

Continuum equation:

$$\frac{\partial(\varepsilon_{\mathrm{i}}\rho_{\mathrm{i}})}{\partial t}+\nabla\cdot(\rho_{\mathrm{i}}\vec{V}_{\mathrm{i}}) = 0 \tag{3}$$

Momentum equation:

$$\frac{\rho_{\mathrm{i}}}{\varepsilon_{\mathrm{i}}}\frac{\partial\vec{V}_{\mathrm{i}}}{\partial t}+\frac{\rho_{\mathrm{i}}}{\varepsilon_{\mathrm{i}}^2}\nabla(\vec{V}_{\mathrm{i}}\cdot\nabla)\vec{V}_{\mathrm{i}} = -\nabla p-\left(\frac{\mu_{\mathrm{i}}}{K}+\frac{\rho_{\mathrm{i}}C}{\sqrt{K}}|\vec{V}_{\mathrm{i}}|\right)\vec{V}_{\mathrm{i}}+\frac{\mu_{\mathrm{i}}}{\varepsilon_{\mathrm{i}}}\nabla^2\vec{V}_{\mathrm{i}} \tag{4}$$

Energy equation:

$$\overline{(\rho c)}_{\mathrm{i}}\frac{\partial T}{\partial t}+\rho_{\mathrm{i}}c_{\mathrm{i}}(\vec{V}_{\mathrm{i}}\cdot\nabla)T = (k_{\mathrm{eff}})_{\mathrm{i}}\nabla^2 T \tag{5}$$

(4) Compensation cavity

Continuum equation:

$$\frac{\partial\rho_{\mathrm{l}}}{\partial t}+\nabla\cdot(\rho_{\mathrm{l}}\vec{V}_{\mathrm{l}}) = 0 \tag{6}$$

Momentum equation:

$$\rho_{\mathrm{l}}\frac{\partial\vec{V}_{\mathrm{l}}}{\partial t}+\rho_{\mathrm{l}}\nabla(\vec{V}_{\mathrm{l}}\cdot\nabla)\vec{V}_{\mathrm{l}} = -\nabla p+\mu_{\mathrm{l}}\nabla^2\vec{V}_{\mathrm{l}} \tag{7}$$

Energy equation:

$$\rho_{\mathrm{l}}c_{\mathrm{l}}\frac{\partial T}{\partial t}+\rho_{\mathrm{l}}c_{\mathrm{l}}(\vec{V}_{\mathrm{i}}\cdot\nabla)T = k_{\mathrm{l}}\nabla^2 T \tag{8}$$

where i = l, v; C is the Forchheimer's constant; (k_{eff}) is the effective thermal conductivity, $(k_{\mathrm{eff}})_{\mathrm{i}} = \varepsilon k_{\mathrm{i}} + (1-\varepsilon)k_s$; $\overline{(\rho c)}$ is the density–capacity heat product defined in the energy equations, $\overline{(\rho c)}_{\mathrm{i}} = \varepsilon\rho_{\mathrm{i}}c_{\mathrm{i}} + (1-\varepsilon)\rho_s c_s$.

The heat transfer in these regions is coupled, and the conservation equations must be solved as a conjugate problem. The boundary conditions of energy and momentum equations can be described below.

Boundary conditions for energy equations:

At $x = 0$:

$$k_{\mathrm{mw}}\frac{\partial T}{\partial x} = 0 \tag{9}$$

At $x = L_x$:

$$\frac{\partial T}{\partial x} = 0 \tag{10}$$

At $y = 0$:

$$k_{\mathrm{mw}}\frac{\partial T}{\partial y} = 0 \quad 0\leqslant x\leqslant L_{x3} \tag{11}$$

$$T = T_{\mathrm{in}} \quad L_{x3}\leqslant x\leqslant L_x \tag{12}$$

At $y = L_y$:

$$k_{\mathrm{mw}}\frac{\partial T}{\partial y} = q \tag{13}$$

The conjugate boundary conditions exist at the interface of two regions. The heat flux and temperatures should be continuous at the interface on both sides.

Boundary conditions for momentum equations:

At $y = 0$:

$$u_l = 0, v_l = 0 \quad 0 \leqslant x \leqslant L_{x3} \tag{14}$$

$$u_l = 0, v_l = v_{in} \quad L_{x3} \leqslant x \leqslant L_x \tag{15}$$

At $y = L_{y3}$:

$$\frac{\partial v_v}{\partial y} = 0 \qquad \text{wick-vapor grooves border in vapor phase region} \tag{16}$$

$$u_i = 0, v_i = 0 \ \text{ other border}, i = v, l \tag{17}$$

At $x = 0$ and $0 \leqslant y \leqslant L_{y3}$:

$$u_i = 0, v_i = 0 \quad i = v, l \tag{18}$$

At $x = L_x$ and $0 \leqslant y \leqslant L_{y3}$:

$$u_i = 0, \frac{\partial v_i}{\partial x} = 0 \quad i = v, l \tag{19}$$

The inlet liquid velocity v_{in} in Eq. (15) at the wick-compensation cavity border can be obtained by performing a overall energy balance on the capillary evaporator.

$$\rho_l v_{in}(L_x - L_{x3})(h_{fg} + c_l \Delta T_{sub} + c_v \Delta T_{sup}) + Q_h = qL_x \tag{20}$$

The left side of Eq. (20) represents the heat absorbed by the working fluid and dissipated heat Q_h of the evaporator by heat convection. The right side of Eq. (20) describes the heat applied at the upper surface of evaporator. ΔT_{sub} and ΔT_{sup} are the subcooling of inlet liquid and the superheating of outlet vapor, respectively. Since the natural convection heat transfer coefficient*h*at the evaporator surface is very low, Q_h can be negligible compared to the applied heat load. The inlet liquid velocity v_{in} is expressed as follow.

$$v_{in} = \frac{qL_x}{\rho_l(L_x - L_{x3})(h_{fg} + c_l \Delta T_{sub} + c_v \Delta T_{sup})} \tag{21}$$

Based on the model of porous media saturated with fluid, the vapor–liquid interface is assumed to have zero thickness inside the wick structure, and the liquid–vapor transition occurs at the interface. Sharp discontinuities of the fluid properties appear across this interface, but continuities of the mass and heat flux should be maintained there.

Mass continuity condition:

$$\rho_l \vec{V}_l = \rho_v \vec{V}_v \tag{22}$$

Energy conservation condition:

$$(k_{eff})_v \nabla T_v \cdot n - (k_{eff})_l \nabla T_l \cdot n = \rho_l \vec{V}_l \cdot n h_{fg} \tag{23}$$

Temperature continuity condition:

$$T_l = T_v = T_{sat} \tag{24}$$

As evaporation takes place inside the wick structure, the capillary menisci are established at the vapor–liquid interface. At the same time, capillary pressure is developed, which draws the liquid through the wick to vapor–liquid interface and circulates the fluid throughout the CPL.

$$\Delta P_c = P_v - P_l = \frac{2\sigma \cos\theta}{r_e} \tag{25}$$

Eq. (24) presents the local thermal equilibrium at the vapor–liquid interface inside the wick structure, and the saturation temperature T_{sat} is equal to the setpoint temperature of two-phase reservoir during normal operating process of CPL. This condition is used to determine the location of vapor–liquid interface. Because the maintenance of a continuous flow of fluid is assured by the capillary pressure of wick, ΔP_c in Eq. (25) should be equal to the total pressure loss in the entire CPL loop.

3. Numerical procedure

The governing equations together with the boundary conditions in the different regions of the evaporator described previous are solved as a conjugate problem with the SIMPLE algorithm which is described in detailed in Ref. [17]. Conjugate problem includes liquid and vapor flow, heat transfer, and phase change in the porous wick structure and liquid flow and heat transfer in the compensation cavity and heat transfer in the vapor grooves and metal outside wall, and these increase the complication of numerical procedure significantly. The additional difficulty here is that the location of the vapor–liquid interface involving phase change is not known. An interface tracking method which is based on the moving structured grid is used to locate the vapor–liquid interface. It indicates that the grid is regenerated at each step.

In order to ensure the convergence of calculating procedure, some technical treatments like under relaxation and error feedback are adopted. The mathematic model mentioned above can predict the transient characteristics of evaporator, but only the steady-state numerical results are discussed in this paper. The overall numerical sequence is described as follows:

(1) Initialize the problem, and choose an initial arbitrary vapor–liquid location inside the wick.
(2) Generate the structured grid in the region of $L_x \times L_{y3}$.
(3) Solve the continuum and momentum equations separately inside region of $L_x \times L_{y3}$.
(4) Regenerate grid inside the entire evaporator.
(5) Solve the energy equations for all regions inside overall evaporator by imposing the energy conservation boundary condition at the interface to obtain the temperature field.
(6) Check whether the temperature condition at the interface is satisfied. If it is not satisfied, the vapor–liquid interface location has to be updated.
(7) Go back to step (2) until convergence.

When the vapor–liquid interface is obtained, the pressure drop across the interface is computed to ensure it is less than the maximum capillary pressure in the wick ($P_v - P_l \leqslant 2\sigma/r_e$). When solving the continuum and momentum equations in the region of $L_x \times L_{y3}$, the numerical technique for solid zone inside the computation domain has been described in detailed in Ref. [18], and it has not represented any more here.

4. Results and discussions

Numerical results are determined for a miniature flat plate evaporator with the following geometric parameters: $L_x = 14$ mm, $L_{x1} = 2$ mm, $L_{x2} = 2.5$ mm, $L_{x3} = 13$ mm, $L_y = 9$ mm, $L_{y1} = 1.5$ mm, $L_{y2} = 4$ mm, and $L_{y3} = 6.5$ mm. The length and height of vapor grooves are 1 and 1.5 mm, respectively. The working fluid is ammonia, and the thermal properties taken in the computation are: $k_l = 0.454\ W\ m^{-1}\ K^{-1}$, $k_v = 0.0302\ W\ m^{-1}\ K^{-1}$, $\mu_l = 2.0 \times 10^{-4}\ N\ s^{-1}\ m^{-2}$, $\mu_v = 1.13 \times 10^{-5}\ N\ s^{-1}\ m^{-2}$, and $h_f = 1.113 \times 10^6\ J\ kg^{-1}$. The sintered stainless steel wick and nickel wick are used in the computation, and the properties for the wick structure are: $k_{st} = 15.2\ W\ m^{-1}\ K^{-1}$, $k_{ni} = 90.4\ W\ m^{-1}\ K^{-1}$, $\varepsilon = 0.6$, and $K = 6.616 \times 10^{-13}\ m^2$. Here aluminum ($k_{al} = 236\ W\ m^{-1}\ K^{-1}$) and stainless steel are chosen as the material of metallic wall, since they are compatible with ammonia. The setpoint temperature is

35 °C, which is the fluid saturated temperatureT_{sat}, and T_{in} = 25 °C. The grid schemes of global evaporator are 142 × 92.

Fig. 4 shows the liquid phase velocity vectors in the evaporator. Fig. 4(a) describes the liquid velocity vectors inside the porous wick, and the magnitude of liquid velocity is 10^{-5}. As seen, the wick structure contains vapor region under the fins separated from the liquid region by the vapor–liquid interface. Naturally, the thin gaps between the fins and upper surface of wick saturated by vapor appear, these gaps allow the vapor to escape from the wick to vapor grooves. The shape of vapor–liquid interface is wavy near the upper surface of wick, and the vapor region is very small. The liquid flows into wick from the wick-compensation cavity border, and is driven to evaporate at the vapor–liquid interface by the wick capillary force. Fig. 4(a) also shows that the liquid evaporation mostly takes place near the upper surface of wick structure, and the liquid velocity is nearly uniform in most liquid zone. At the same time, because of heat conduction effect of side metallic wall, the liquid evaporation also occurs in the vicinity of left-hand surface of wick. Since the vapor zone is very small, the vapor velocity vectors are not given in this paper. Fig. 4(b) presents the results for the liquid velocity vectors in the compensation cavity. As seen, the velocity near the inlet is uniform along the flow direction, and far from the inlet, the velocity decreases gradually. Due to liquid evaporation occurs mostly in the vicinity of the upper surface of wick, the liquid nearly uniformly enters the wick from compensation cavity, as shown in Fig. 4(b).

Fig. 5 shows the temperature distributions of the evaporator for different heat fluxes. Because of great difference in thermal conductivity between the metallic fins and vapor, heat is transferred to wick mainly by conduction of the fins, and the shape of isotherms near the upper surface of wick structure is wavy. The shape of vapor–liquid interface where the temperature contour level is equal to the saturated temperature of 35 °C inside the wick is also wavy, and it is mainly determined by the geometric parameters of fins and vapor grooves. The vapor–liquid interface locates in the vicinity of the upper and left surface of wick structure, as has been observed by the visualization experiment of Zhao et al. [19]. When the heat flux is increased, the vapor–liquid interface inside the wick moves away from the fins and the size of the vapor zone and the gaps enlarges, these can be found in Fig. 5(b). Due to high thermal conductivity of aluminum, the temperature gradients inside the metallic wall are very small, which means the temperatures of the evaporator heated surface are almost uniform.

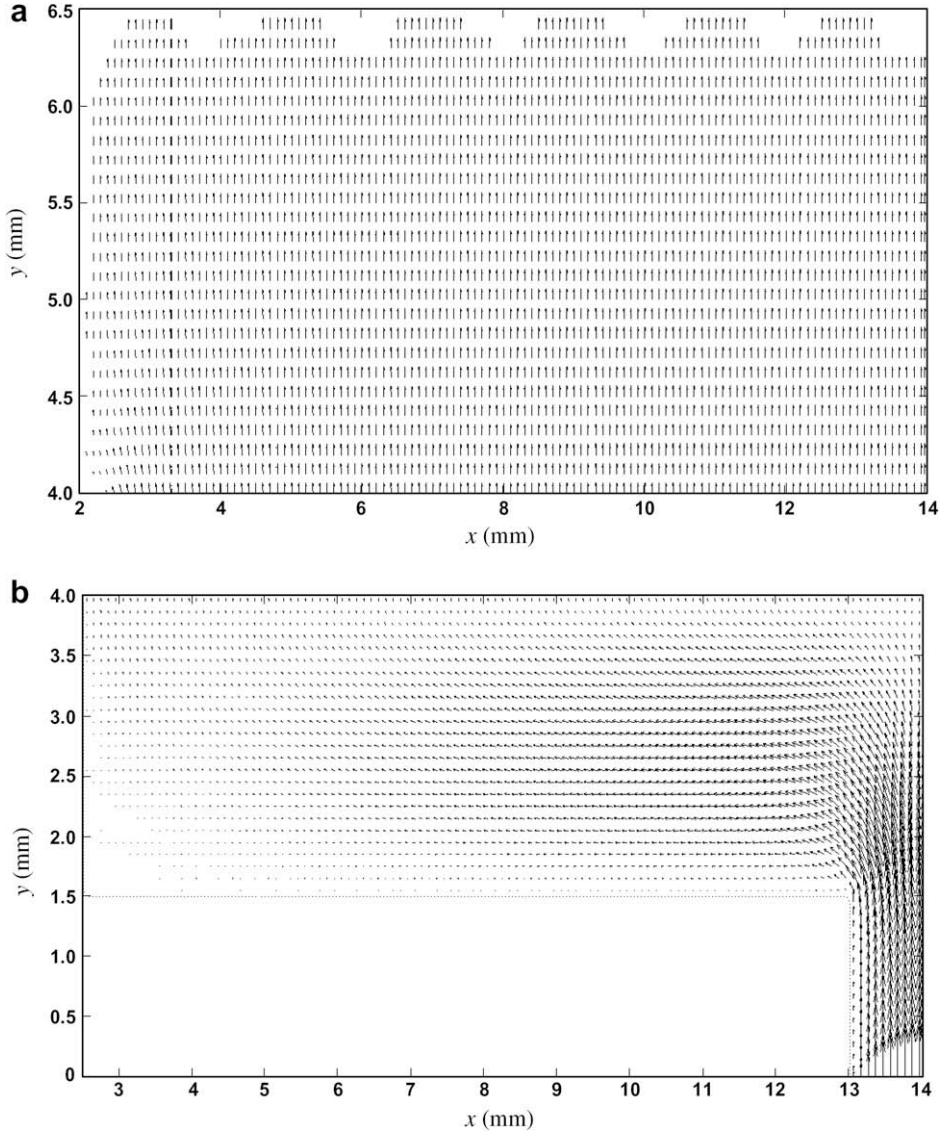

Fig. 4. Liquid velocity vectors (aluminum wall, stainless steel wick, $q = 4 \times 10^4$ W m^{-2}, ΔT_{sub} = 10 °C). (a) In the wick structure and (b) in the compensation cavity.

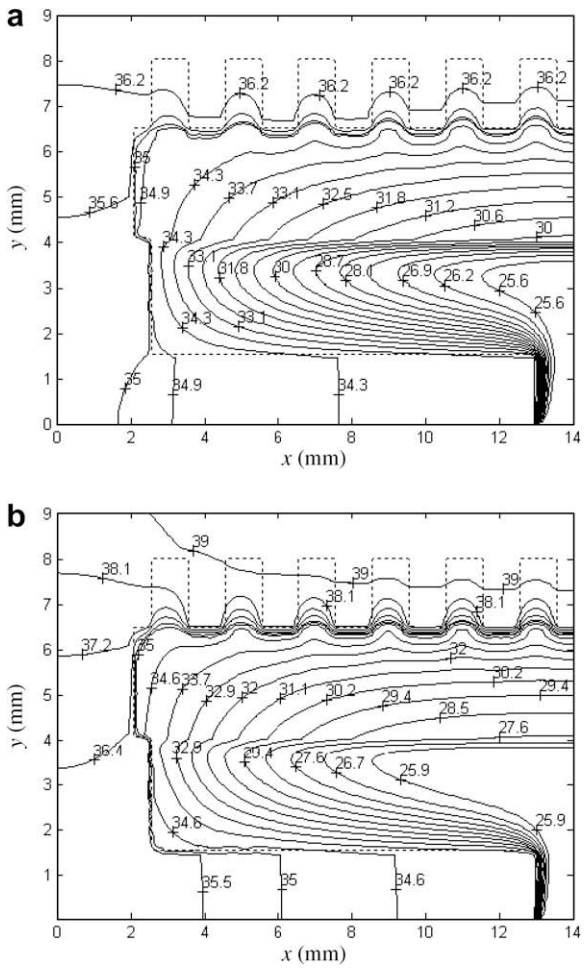

Fig. 5. Temperature fields (aluminum wall, stainless steel wick, $\Delta T_{sub} = 10\ ^{\circ}C$). (a) $q = 4 \times 10^4\ W\ m^{-2}$ and (b) $q = 8 \times 10^4 W \cdot m^{-2}$.

Because the thickness of side wall cannot be negligible for the miniature flat plate evaporator, the influence of heat conduction of side metallic wall on heat transport capacity needs to be considered. At heat flux of $q = 4 \times 10^4\ W\ m^{-2}$, because k_{al} is large more than k_{st}, the left vapor–liquid interface (contour level of 35 °C) goes deeply into the left bottom surface of compensation cavity, which reveals that it is safe for CPL normal operation. With the increases of heat flux, the influence of heat conduction of side wall on the vapor–liquid interface is very significant. As shown in Fig. 5(b), the isotherm of 35 °C has invaded deeply into the bottom of the compensation cavity, which indicates that the vapor may be generated there under this condition, and the vapor presence in there can fully or partially block liquid to vapor–liquid interface to evaporate and results eventually in dry-out of the evaporator. For a miniature flat plate CPL evaporator, if the thermal conductivity of side wall is larger than the effective thermal conductivity of wick, the effect of heat conduction of side wall leads to the day-out of evaporator, this is considered as a heat transfer limit, called side wall effect heat transfer limit here. It is a very important heat transfer limit compared to other heat transfer limits of CPL, and this is great difference between flat plate CPL and cylindrical CPL. Because of existence of the side wall effect heat transfer limit for the miniature flat plate CPL, evaporator with single aluminum wall cannot transport very high heat flux.

The heated surface of the evaporator is directly attached to the apparatus, and high and uneven temperatures of heated surface may result in abnormality of the apparatus. Consequently, the temperature level and isothermal characteristic of heated surface is a very important parameter to estimate the performance of CPL evaporator.

Fig. 6 shows the temperature profiles in the different plane of evaporator along *x*-direction. As seen, the heated surface temperatures increase with the applied heat fluxes. Because of high thermal conductivity of aluminum, the heated surface temperature level is low, even though at $q = 8 \times 10^4\ W\ m^{-2}$, the maximum temperature is less than 40 °C. At the same time, the heated surface temperature is nearly uniform for uniform heat flux and the temperature difference along heated surface is less than 1.5 °C. Not surprisingly, these are favorable for cooling apparatus, which indicate that the metallic wall with high thermal conductivity can effectively decrease the heated surface temperatures and maintain the good isothermal characteristic of the heated surface. In the plane of $y = 4 \times 10^{-3}$ m, the temperature (about $x < 2.5 \times 10^{-3}$ m) increases with the applied heat fluxes increasing, but the temperature at the border of wick-compensation cavity decreases with the applied heat fluxes increasing, which can be explained that high heat flux leads to high liquid velocity in the compensation cavity, the liquid has not been heated up to a high temperature level before it arrives the wick inlet. As a result, increasing the heat flux decreases the temperature at the inlet of wick.

Fig. 7 presents the influence of inlet liquid subcooling on the temperature of evaporator at $q = 8 \times 10^4\ W\ m^{-2}$. Compared with

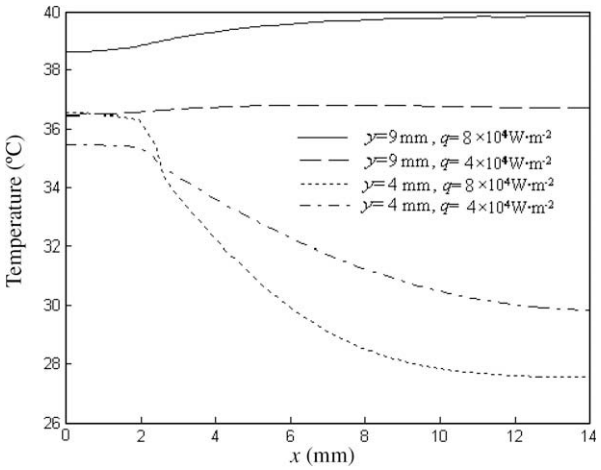

Fig. 6. Temperature distributions in the different plane (aluminum wall, stainless steel wick, $\Delta T_{sub} = 10\ ^{\circ}C$).

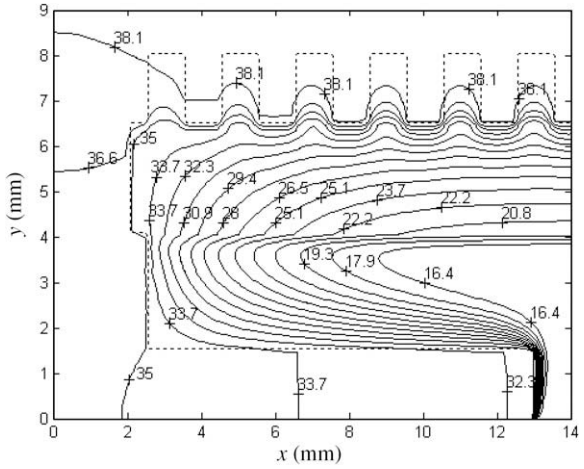

Fig. 7. isotherms in the evaporator (aluminum wall, stainless steel wick, $\Delta T_{sub} = 20\ ^{\circ}C$).

Fig. 5(b), it can be found that increasing the inlet liquid subcooling increases the temperature gradients inside the wick. Due to heat convection of liquid with lower temperature in the compensation cavity and wick, high subcooling aids in preventing vapor formation in the compensation cavity and inside the bottom wick, and it is favorable for normal operation of CPL. Furthermore, Fig. 7 also shows the left vapor–liquid interface locates near the bottom left corner of compensation cavity, and the isotherm of saturated temperature has not invaded deeply into the bottom surface of the compensation cavity. Therefore, increasing the liquid subcooling can enhance the side wall effect heat transfer limit of the evaporator and help to increase the safety of miniature flat plate CPL.

To evaluate the influence of thermal conductivity of wick on the performance of evaporator, the sintered nickel wick is used as a material of high thermal conductivity in the computation. Fig. 8 shows the temperature distributions in the evaporator with nickel wick. Compared to evaporator with sintered stainless steel wick (Fig. 5b), as seen from Fig. 8, heat conduction of side wall decreases correspondingly, and the left vapor–liquid interface locates at the left surface of compensation cavity and the isotherm of saturated temperature has not invaded deeply into the compensation cavity. Because of high thermal conductivity of nickel wick, the heat conduction to the compensation cavity through the wick increases, and the temperature gradients are small and the liquid in the compensation cavity is heated to a higher temperature level. Fig. 9 shows the temperature difference between saturated temperature and bottom wick surface temperature along x-direction for different material wick. The temperature difference for stainless steel wick is much greater than that for nickel wick, and lower temperature difference is found to increase the chance of an eventual evaporator deprime [20].

In order to investigate the effects of wall material on the performance of evaporator, the stainless steel wall and combined wall (upper wall material is aluminum, side and bottom wall material is stainless steel) are also used in the computation. Fig. 10 shows the temperature distributions in the evaporator with different wall material at $q = 12 \times 10^4$ W m^{-2}. As shown in Fig. 10(a), due to low thermal conductivity for stainless steel wall, the temperature gradients are very large in the upper wall zone, and decrease in the wick and bottom wall zone. At the same time, deleterious effects of heat conduction of side wall decreases, and the isotherm of saturated temperature has not invaded deeply into the compensation cavity bottom, the CPL can operate safely under this condition. As shown in Fig. 10(b), because of high thermal conductivity of upper

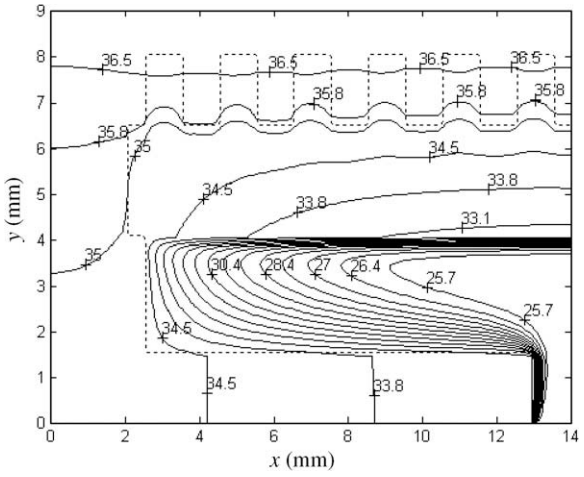

Fig. 8. Temperature fields (aluminum wall, nickel wick, $\Delta T_{sub} = 10$ °C, $q = 8 \times 10^4$ W m^{-2}).

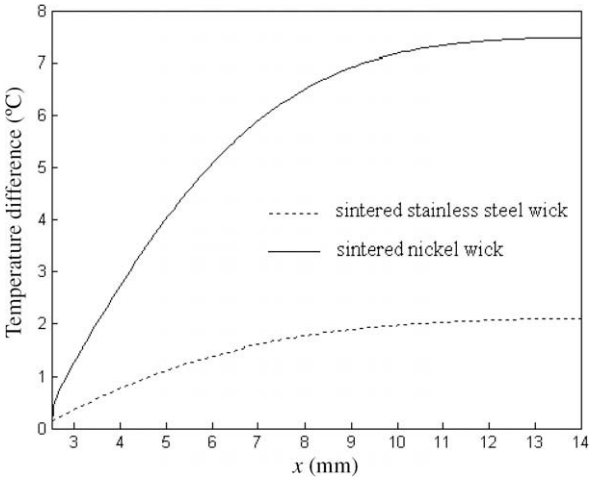

Fig. 9. Temperature difference between saturated temperature and bottom wick surface temperature (aluminum wall, $\Delta T_{sub} = 10$ °C, $q = 8 \times 10^4$ W m^{-2}).

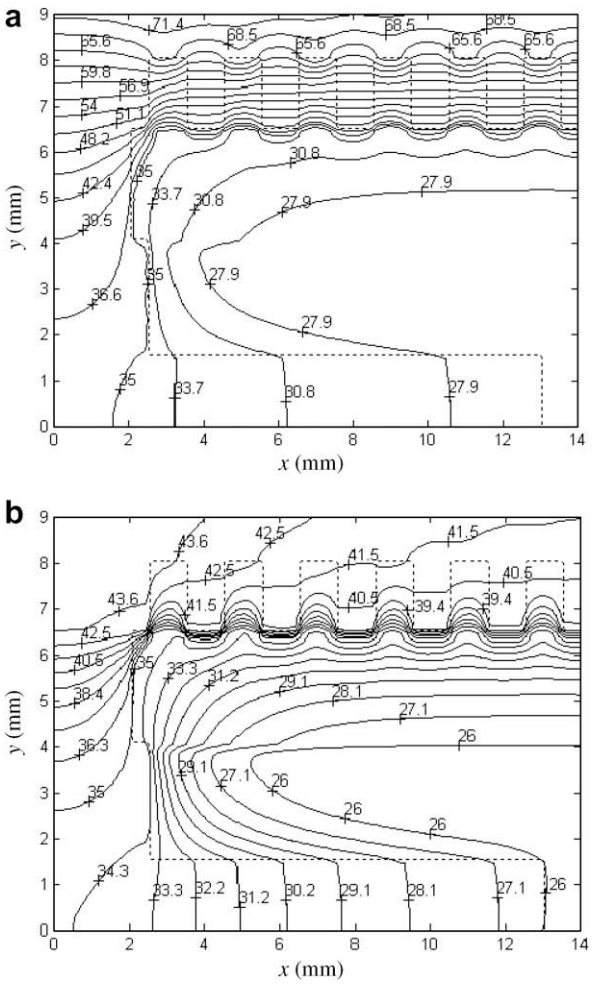

Fig. 10. Isotherms in the evaporator (stainless steel wick, $\Delta T_{sub} = 10$ °C). (a) Stainless steel wall and (b) combined wall.

wall, the temperature gradients are small in the upper wall zone, but temperature gradients are large inside the wick and side and bottom wall. The effect of heat conduction of side wall is obviously less, and the isotherm of saturated temperature only arrives at the left bottom wick surface, which indicates that CPL has not reached

the side wall effect heat transfer limit. As discuss above, it indicates that side wall with low thermal conductivity is more suitable for dissipating high heat fluxes. On the other hand, at $q = 12 \times 10^4\ W\ m^{-2}$, the heated surface temperature of evaporator with stainless steel wall is more than 71.4 °C, which is deleterious for the normal operation of cooled apparatus. But the heated surface temperature of evaporator with combined wall is about 43.6 °C, it is moderate for the cooled apparatus, and the temperature distribution along the heated surface is more uniform. Under this condition, the cooled apparatus can operate effectively and have a long life. Thereby, the thermal conductivity of wall has a significant influence on the performance of miniature flat plate CPL evaporator, and upper wall with high thermal conductivity results in low temperature and good isothermal characteristic of heated surface. The flat plate evaporator with combined wall improves the heat transport capacity and maintains an appropriate temperature level of the heated surface.

The heat distribution induced by cooled apparatus is not always uniform during their normal operations, and the effect of non-uniform heat flux needs to be assessed. In the numerical computation, it assumes that the heat flux distribution varies along the heated surface as follow:

$$q(x) = 10^4 \cdot [16 - 12(x/l_x - 1)^2] \quad (26)$$

Fig. 11 shows the temperature distribution in the evaporator with different wall material in the case of non-uniform heat flux. As seen, for the non-uniform heat flux, the isotherm of saturated temperature in the evaporator with stainless steel wall or combined wall has not invaded into the compensation cavity, which indicates the capillary evaporator operates safely in the case of non-uniform heat flux. Fig. 12 presents the effect of non-uniform heat flux on the heated surface temperature. In the case of stainless steel wall, the shape of heated surface temperature is wavy due to the effect of vapor grooves. As expected, the peak temperature occurs at the center of heated surface where the heat flux is maximal. In the case of the stainless steel wall, because of low thermal conductivity, the maximal temperature is higher than 84 °C, and the peak temperature difference on the heated surface is more than 28 °C. High temperature and large temperature difference along the heated surface may result in short-life of the cooled apparatus. However, in the case of combined wall, the heated surface temperature is moderate and almost uniform, which implies that evaporator with the combined wall has more strong ability to accommodate the non-uniform heat flux than that with stainless steel wall.

5. Conclusions

An overall model for the miniature flat plate CPL evaporator is presented, which includes liquid and vapor flow, heat transfer and phase change in the porous wick structure, liquid flow and heat transfer in the compensation cavity and heat transfer in the vapor grooves and metallic wall. The governing equations for different zones are solved numerically as a conjugate problem.

The liquid evaporation takes place near the upper and left surface of wick structure in the evaporator, and with the increases of the applied heat fluxes, the vapor–liquid interface moves away from the fins and the size of the vapor zone enlarges. On the other hand, lower temperature liquid exists at the entrance of wick at higher heat flux, and convection of lower temperature liquid helps to prevent the vapor formation inside the bottom wick. For the miniature flat plate CPL evaporator, the effect of heat conduction of side metallic wall on the behaviors of evaporator is great, and side wall effect heat transfer limit is introduced to estimate the heat transport capacity of the evaporator. Due to the existence of side wall effect heat transfer limit, the evaporator with aluminum wall has a low heat transport capability. Increasing the inlet liquid subcooling helps to prevent the vapor formation inside the compensation cavity and the bottom wick structure and also increases the side wall effect heat transfer limit. The evaporator with high

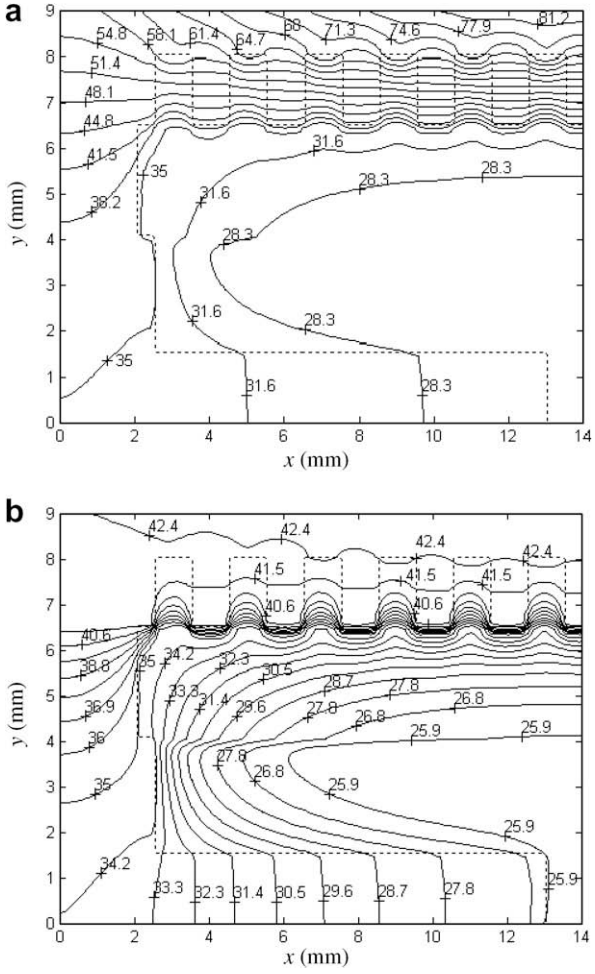

Fig. 11. Temperature fields for non-uniform heat flux (stainless steel wick, ΔT_{sub} = 10 °C). (a) Stainless steel wall and (b) combined wall.

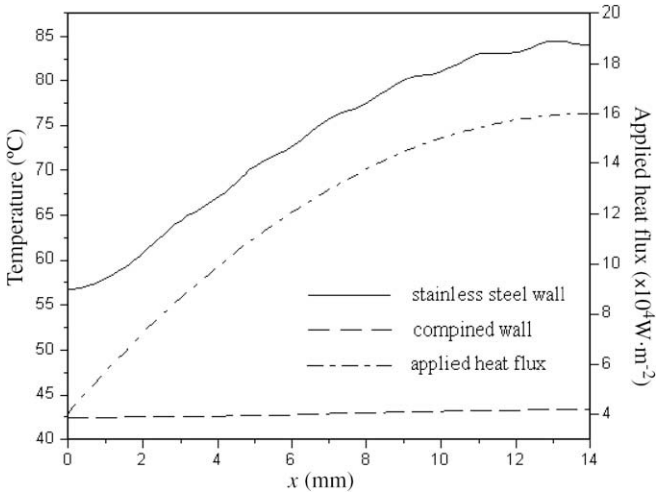

Fig. 12. Temperature distributions along heat surface for non-uniform heat flux (stainless steel wick, ΔT_{sub} = 10 °C).

thermal conductivity wick, such as nickel wick, can improve the side wall effect heat transfer limit, but increases the chance of an eventual evaporator deprime. The flat plate evaporator of single aluminum wall results in lower side wall effect heat transfer limit, but leads to lower temperature level and good isothermal behavior of the heated surface. On the other hand, the evaporator with single stainless steel wall leads to higher heat transport capacity, but to higher temperature level of the heated surface. The evaporator with combined wall (upper wall with aluminum, side and bottom wall with stainless steel) increases side wall effect heat transfer limit, and maintains an appropriate temperature level and good isothermal characteristic on the heated surface and enhances the ability to accommodate the non-uniform heat flux, which imply that the CPL can operate safely and cooled apparatus can also work effectively under higher heat fluxes and non-uniform heat fluxes.

The present overall numerical model of miniature flat plate CPL evaporator can effectively estimate the heat transfer capacity of evaporator and evaluate the temperature level of the heated surface, and it is useful for the evaporator design and performance optimization of miniature flat plate CPL.

Acknowledgement

The current work is supported by the National Key Basic Research Development Program of China (No. 2007CB206901).

References

[1] R. Nadalini, F. Bodendieck, The thermal control system for a network mission on Mars: The experience of the Netlander mission, Acta Astronautica 58 (11) (2006) 564–575.
[2] T.D. Swanson, G.C. Birur, NASA thermal control technologies for robotic spacecraft, Applied Thermal Engineering 23 (9) (2003) 1055–1065.
[3] S. Clayton, D. Martin, J. Baumann, Mars surveyor thermal management using a fixed conductance capillary pumped loop, SAE Paper No.972467, 1997.
[4] M. Nikitkin, B. Cullimore, CPL and LHP technologies: what are the differences, what are the similarities? SAE Paper No.981587, 1998.
[5] D. Butler, L. Ottenstein, J. Ku, Design evolution of the capillary pumped loop (CAPL-2) flight experiment, SAE Paper No.961431, 1996.
[6] T. Hoang, J. Ku, Hydrodynamic aspect of capillary pumped loop, SAE Paper No.961435, 1996.
[7] E. Pouzet, J.L. Joly, V. Platel, et al., Dynamic response of a capillary pumped loop subjected to various heat load transients, International Journal of Heat and Mass Transfer 47 (10) (2004) 2293–2316.
[8] P.C. Chen, W.K. Lin, The application of capillary pumped loop for cooling of electronic components, Applied Thermal Engineering 21 (11) (2001) 1739–1754.
[9] E. Bazzo, R.R. Riehl, Operation characteristics of a small-scale capillary pumped loop, Applied Thermal Engineering 23 (6) (2003) 687–705.
[10] S. Randeep, A. Aliakbar, D. Chris, et al., Miniature loop heat pipe with flat evaporator for cooling computer CPU, IEEE Transaction on Components and Packaging Technologies 30 (1) (2007) 42–49.
[11] I. Muraoka, F.M. Ramos, V.V. Vlassov, Experimental and theoretical investigation of a capillary pumped loop with a porous element in the condenser, International Communications in Heat and Mass Transfer 25 (8) (1998) 1085–1094.
[12] Y. Cao, A. Faghri, Analytical solutions of flow and heat transfer in a porous structure with partial heating and evaporation on the upper surface, International Journal of Heat and Mass Transfer 37 (10) (1994) 1525–1553.
[13] A.S. Demidov, E.S. Yatsenko, Investigation of heat and mass transfer in the evaporation zone of a heat pipe operating by the 'inverted meniscus' principle, International Journal of Heat and Mass Transfer 37 (14) (1994) 2155–2163.
[14] C. Figus, Y.L. Bray, S. Bories, et al., Heat and mass transfer with phase change in a porous structure partially heated: continuum model and pore network simulations, International Journal of Heat and Mass Transfer 42 (14) (1999) 2557–2569.
[15] Y.H. Yan, J.M. Ochterbeck, Numerical investigation of the steady-state operation of a cylindrical capillary pumped loop evaporator, Journal of Electronic Packaging 125 (2) (2003) 251–260.
[16] J. Ku, Start-up issues of capillary pumped loops, Proceedings of the Nineth International Heat Pipe Conference, Albuquerque, NM, 1995, pp. 994–1001.
[17] W.Q. Tao, Numerical Heat Transfer, Xi'an Jiao Tong University Press, Xi'an, China, 2001 (in Chinese).
[18] M. Yang, W.Q. Tao, Three-dimensional natural convections in an enclosure with an internal isolated vertical plate, ASME Journal of Heat Transfer 117 (1995) 619–625.
[19] T.S. Zhao, Q. Liao, On capillary-driven flow and phase-change heat transfer in a porous structure heated by a finned surface: measurements and modeling, International Journal of Heat and Mass Transfer 43 (4) (2000) 1141–1155.
[20] J.L. Tim, M. Issam, Thermal transients in a capillary evaporator prior to the initiation of boiling, International Journal of Heat and Mass Transfer 43 (21) (2000) 3937–3952.